Chemical Species Tomography of Carbon Dioxide

Tsekenis S-A[1*], Polydorides N[1], Fisher E[1], Chighine A[1], Jiabin J[1], McCann H[1]
Wilson D[2], Humphries G[2], Lengden M[2], Benoy T[2], Johnstone W[2]
Kliment J[3], Wright P[3], Feng Y[4], Nilsson LJ[4], Victor DA Prat[5]

[1] School of Engineering, The University of Edinburgh, Edinburgh, UK
[2] Centre for Microsystems & Photonics, University of Strathclyde, Glasgow, UK
[3] The University of Manchester, Oxford Road, Manchester, UK
[4] Optoelectronics Research Centre, University of Southampton, Highfield, Southampton, UK
[5] INTA Turbojet Engine Test Centre, Torrejón de Ardoz (Madrid), Spain

*a.tsekenis@ed.ac.uk

Abstract

In this paper we report on the first tomographic reconstructions of CO_2 concentration distributions created by gaseous phantoms. The tomography system has been developed as part of project FLITES which aims to provide images of various target chemical species within the exhaust plume of turbine engines. We provide a brief overview of the instrumentation system and a detailed description of the phantom apparatus. Data analysis and image reconstruction of the data is discussed and the first preliminary reconstructions are presented. The presented results from imaging gaseous phantoms validate the successful design, correct configuration and operation of the entire data collection, analysis and processing chain prior to the in-situ experiments using an aero-engine.

Keywords: tomography, image reconstruction, spectroscopy, aero-engine, carbon dioxide, emission diagnostics

Conference Topic: Applications of industrial process tomography

1. Introduction

The FLITES consortium (Fibre-Laser Imaging of gas Turbine Exhaust Species) aspires to enhance the turbine-related research and contribute to the low-carbon development based on e.g. biofuels. The aim of the project is to introduce advanced laser-based combustion diagnostic techniques to the turbine engine environment in order to access the exhaust plume chemistry targeting, in the first instance, CO_2 and soot. The readers are encouraged to visit the consortium's website, www.flites.eu.

In this paper we focus on the commissioning of the CO_2 imaging system. The system has been assembled outside the engine test cell and at the time of writing lies horizontally on the ground at the turboreactor facility of the Instituto Nacional de Tecnica Aeroespacial (INTA) near Madrid. Whilst at this position, a series of tests have been conducted to ensure correct operation of the entire system prior to its move inside the engine test cell. In this paper we present the high-level testing of the CO_2 system using gaseous phantoms to emulate the exhaust of the turbine engine. The ability to successfully reconstruct known CO_2 concentration distributions demonstrates the correct operation of the imaging system and its sub-components.

2. Tomography system

The tomography system has been described in detail in previous publications. The design and performance of the opto-mechanical systems has been published in [2] whereas a review of in-situ measurement of CO_2 in aerospace engines can be found in [3].

The tomography system has been designed to be located approximately 4 m behind the aero-engine exhaust nozzle and comprises 126 beams arranged in 6 projections with an angular separation of 30° (Figure 1b). Each projection comprises 21 parallel beams with each beam formed by individual launch and receive optical elements (42 elements per projection). The elements are affixed on supporting alignment plates on each segment of a 7 m-diameter dodecagon 'ring' structure (Figures 1a and 2). The support plates of a given projection are made co-planar and parallel to each other using optical alignment means. The alignment of individual beams was optimised using kinematic mounts. The main region of interest where the majority of exhaust CO_2 is expected to be present is approximately 1.4 m in diameter. The pitch of the beams within each projection is 75 mm, thus sampling a linear distance of 1.5 m which is also the diameter of the imaging space.

The optical source is a WMS-modulated seed laser operating near 2 µm and a Thulium Doped Master Oscillator Power Amplifier (TD-MOPA). The light source provides up to 2.5 W of optical power that is split into 126 transmission channels using fibre-splitters and delivered to an equal number of free-space launch elements that create collimated laser beams across the ring. Extended InGaAs photodiodes are used in custom receiver modules.

The data acquisition system simultaneously captures and processes the raw signals from the 126 amplified detectors at 40 MS/s with 14 bit resolution and integrated hardware lock-in amplifiers. A detailed account on the design of the acquisition system through the entire signal chain has been separately submitted to this congress [5]. In order to be able to present the first results at this congress, we utilised a number of commercial components (National Instruments) to create an 8 channel, 2 MS/s, 16 bit acquisition system. The lock-in detection, filtering and presentation were implemented in software.

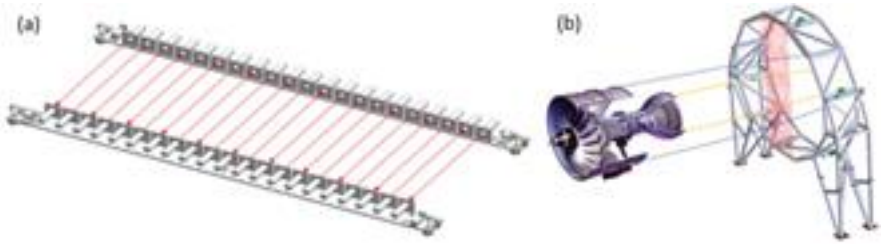

Figure 1: Design rendering of an opposing pair of optical alignment plates supporting 21 parallel beams and forming one tomographic projection (a). Schematic representation of the location and orientation of the structural ring with respect to the engine exhaust (b).

Figure 2: Tomography system for imaging CO_2 concentration distribution at the exhaust of an aerospace engine. The 12 optical alignment plates and individual launch/receive optical elements are visible on the ring's segments.

3. In-situ gaseous phantom trials

Commissioning experiments where performed using gaseous phantoms to emulate the turbofan engine exhaust. The experiments were performed with the ring in the horizontal position and outside the engine test cell.

3.1. CO_2 phantoms

The experimental apparatus comprised two circular CO_2 'generators', the phantoms, of diameter d_1 = 40 cm and d_2 = 60 cm (Figure 3a). Given the imaging space diameter D = 1.4 m, the phantoms correspond to $d_1 \equiv D/3.5$ and $d_2 \equiv D/2.3$.

The phantoms' operation is straightforward. For each phantom, an annular propane burner is located at the bottom of a 1 m long exhaust pipe (Figure 3b). The burner creates CO_2 as a by-product of propane combustion (approximately 11% v/v from a stoichiometric mixture). The energy released from the exothermic reaction heats all combustion by-products making them rise inside the exhaust pipe. The pipe helps to homogenise the CO_2 distribution before releasing it approximately 10 cm below the imaging plane (Figure 4). The diameter of the plume is dtermined by the diameter of the homogenising pipe.

Testing of the phantoms' output showed that, with the design described above, the maximum achievable CO_2 concentration and temperature were approximately 1% v/v at 100 °C. The WMS signal generated from this concentration over a path-length of 40-60 cm was difficult to distinguish from the background CO_2 signal generated over the 7 m path-length between the launch and receive elements. The relatively low CO_2 concentration was due to a large volume of ambient air being entrained into the exhaust pipe in combination with a lean propane/air mixture in the burner.

To raise the concentration of CO_2 in the exhaust plume, the bottom of the homogenising pipe was sealed-off to prevent entrainment of ambient air. Additionally, an external CO_2 cylinder was connected to gas inlets inserted at the bottom and inside of the phantoms (Figure 3b). The partial vacuum created by the hot rising combustion by-products draws the injected CO_2 towards the exhaust. The amount of additional CO_2 introduced in the phantom was regulated to prevent extinction of the burner flame.

Testing of the enhanced phantoms was done by sampling the plume CO_2 concentration and temperature across the exhaust of each phantom using an extractive flue gas analyser (KANE model 455). The spatial average was approximately 6% v/v CO_2 at 230 °C which presented a sufficiently strong spectroscopic absorption signal for subsequent analysis.

3.2. Experimental procedure

Collection of experimental data was performed in a number of steps. Initially, the background CO_2 concentration was acquired. Subsequently, the phantoms were positioned, activated, adjusted and allowed to settle for 2 minutes. Finally, the background CO_2 levels after the experiment were acquired in the absence of phantoms. Throughout the day the laser source was characterized to ensure that any drifts in its operating characteristics are later compensated for.

Data was collected from each projection manually, 8 channels at a time, using the commercial data acquisition system described in Section 2. Each experimental step, including background acquisition, required data from all 126 channels to be collected over a period of 20 minutes.

The datasets selected for the experimental campaign succeeded in presenting each beam of the array with a concentration of CO_2, thereby fully testing the installed system prior to the engine tests. The datasets are tabulated in Table 1.

Dataset	Description	Imaging space
1	40 cm phantom at centre of imaging space	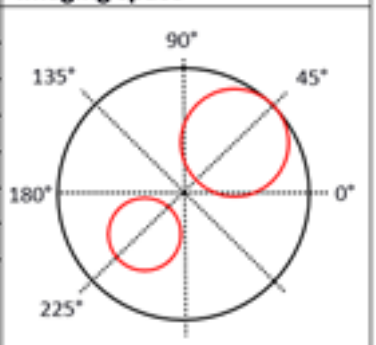
2	60 cm phantom -//-	
3	40 cm phantom at 0°	
4	40 cm phantom at 45°	
5	40 cm phantom at 90°	
6	40 cm phantom at 135°	
7	40 cm phantom at 180°	
8	Dual phantom (see diagram on the right): 60 cm phantom at 45°, edge of imaging space 40 cm phantom at 225°, 20 cm separation	

Table 1: Datasets collected as part of the experimental campaign using gaseous phantoms.

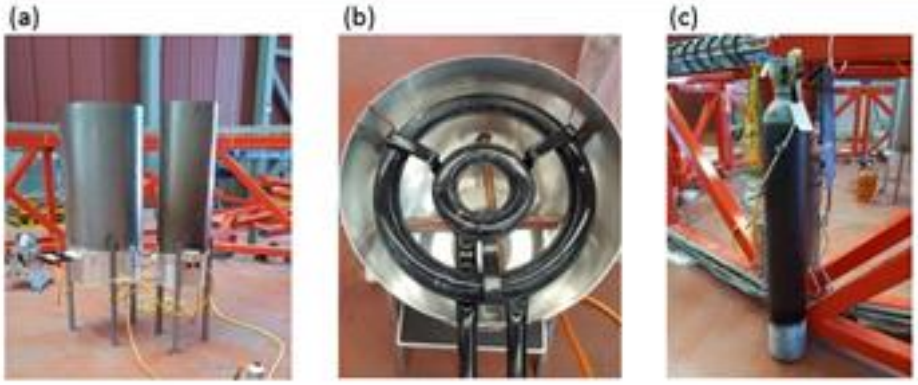

Figure 3: Gaseous phantom apparatus. (a) 40 and 60 cm phantoms set for acquisition, (b) propane burner and auxiliary gas inlets below, (c) CO_2 tank to augment phantom output.

Figure 4: Top of gaseous phantom and launch/receive optical elements showing placement of exhaust approximately 10 cm below the imaging plane.

4. Data analysis

The data processing interface between spectroscopic analysis and data acquisition has been briefly presented in [6]. For each experimental dataset (Table 1), raw data was captured from all 126 detectors over a period of 10 s. The captured signals were averaged over the acquisition period. The in-phase and quadrature components (denoted *X* and *Y* respectively) at the *1f* and *2f* frequencies were generated by

a lock-in detector implemented in software. To achieve demodulation the lock-in detector utilised an in-phase and a quadrature reference signals (denoted by *Ref* and *Ref + π* respectively). The filter of the lock-in detector was an Infinite Impulse Response (IIR) Low Pass Filter (LPF) with a time constant of 0.5 ms. The demodulated *1f* signal vectors *X1F* and *Y1F* were summed yielding the *1f* reference signal *R1F*. The same process was repeated for acquiring the *1f* background reference signal $R1F_{bk}$.

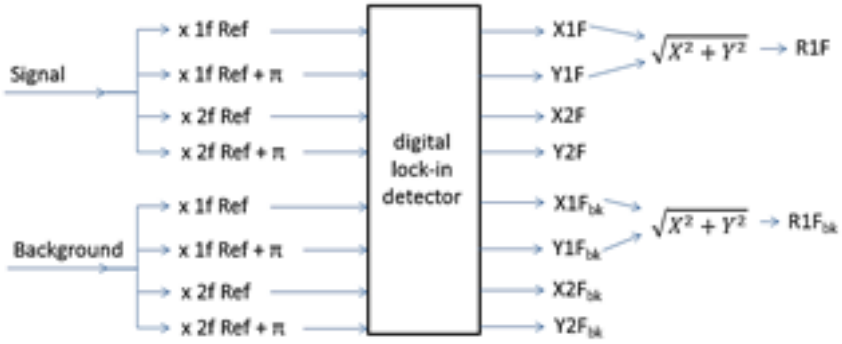

Figure 5: Block-diagram representation of the data processing algorithm to condition the raw data acquired from the 126 detectors on the structural ring. In-phase components are denoted by *X* and quadrature components by *Y*.

The final *1f*-normalised and background-compensated *2f* signal was computed according to equation 1 and subsequently fitted to the spectroscopic model to yield the concentration of CO_2. An example of the *2f/1f* signal is shown in Figure 6 for 8 channels, 3 of which interact with the CO_2 plume.

$$2f/1f = \sqrt{\left[\left(\frac{X2f}{R1f}\right) - \left(\frac{X2f_{bk}}{R1f_{bk}}\right)\right]^2 + \left[\left(\frac{Y2f}{R1f}\right) - \left(\frac{Y2f_{bk}}{R1f_{bk}}\right)\right]^2} \qquad (1)$$

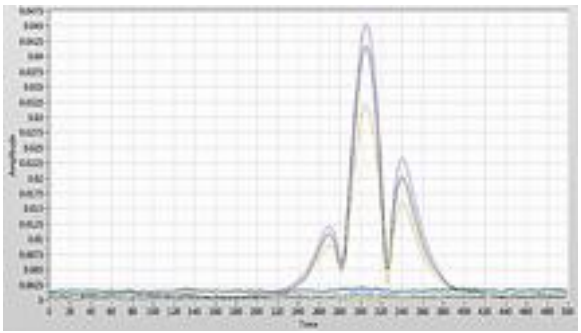

Figure 6: Final *2f/1f* signal of 8 beams following background compensation. Three beams interact with the CO_2 plume from the phantoms.

5. Image reconstruction

The image reconstruction algorithms fundamentally attempt to infer the distribution of the absorbing species, here CO_2, ideally based solely on the measured path-integrated concentration values i.e. without other information. If an infinite number of beams at an infinite number of angles can be employed, then original distribution can be reconstructed unambiguously. However, in practical tomography systems the number of beams and angles are limited and so the image to be reconstructed contains more unknowns (degrees of freedom) than available data. It is said that the inversion problem is ill-posed and the solutions (reconstructed images) are not readily unique. In this case some additional, *a priori* information about the solution is taken into consideration to enforce regularisation and make

the solution to the inverse problem tractable. The prior assumptions when imaging gaseous distributions are typically smoothness and non-negativity i.e. the concentration varies smoothly in the imaging space and cannot be negative.

In this work both the smoothness and non-negativity assumptions have been incorporated into the image reconstruction algorithms. A detailed presentation of the algorithms used has been previously published [1] and only a brief explanation is provided here.

5.1. Smoothness-imposing algorithm

At a high-level, the smoothness-imposing algorithm transforms the high-dimensional, highly detailed image of the concentration distribution into a low-dimensional set of basis function that capture the dominant features of the image. In other words, the high-dimensional space is re-parametrised and projected onto a low-dimensional space. The projection operation causes some loss of information thus introducing an approximation error but the resulting inversion problem can be solved efficiently.

Choice of the basis functions is critical in the image reconstruction process. In this work 144 discrete cosine basis functions were used to, in combination with the 126 measurements, form the low-dimensional space. The functions are of increasing frequency so that the n^{th} function has a frequency n times that of $n = 1$. The size of the basis intrinsically assumes some level of smoothness in the solution.

Following projection in the low-dimensional space, the projected inverse problem is solved numerically using Tikhonov regularisation. The solution introduces a computational error.

The process can be shown diagrammatically [1] in equation 2:

$$c^* \xrightarrow[\text{error}]{\text{approximation}} \Pi c^* = \Phi r^* \xrightarrow[\text{error}]{\text{computational}} \Phi \hat{r}, \qquad (2)$$

Where c^* is the high-dimensional image, Π is the orthogonal low-dimensional space operator, Φ is the matrix of basis functions and r is the computed solution (the reconstructed image). This algorithm is not iterative.

5.2. Positivity-imposing algorithm

The positivity-imposing algorithm [1] prevents the solution from containing negative concentration values. The non-negativity is imposed by reformulating the forward model (based on the Beer-Lambert law) such that the concentration is expressed as a logarithm in equation 3:

$$y = Ac \xrightarrow{z=\log(c)} y = Ae^z \qquad (3)$$

where y is the measured noise-free concentration values, A is the sensitivity matrix and c is the actual concentration. The algorithm proceeds to linearise the reformulated model around a point z_i and projects the model to a low-dimensional space similarly to the smoothness-imposing algorithm. The positively-constrained image of the concentration distribution can be obtained iteratively as described in [1].

6. Preliminary results

In this section we present image reconstructions using experimental data from the datasets described in section 3. These preliminary images are the first images to be produced using the tomography system.

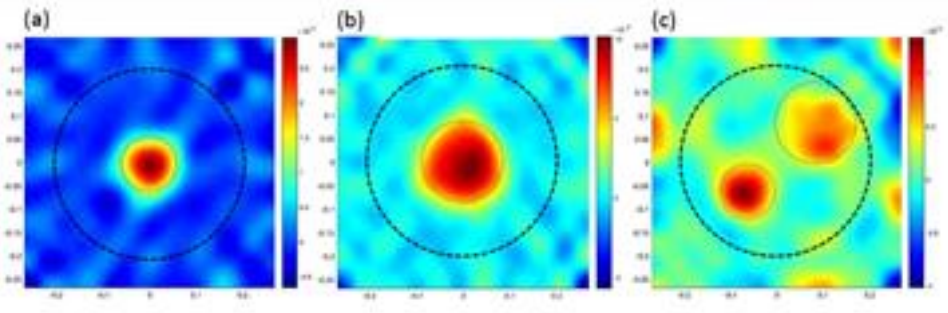

Figure 7: Preliminary image reconstructions using the smoothing algorithm. (a) is the 40 cm (b) is the 60 cm phantoms (white circles) at the centre of the imaging space (black circle). (c), both phantoms at 45˚ from the x-x' axis and spaced by approximately 20 cm. Experimental data.

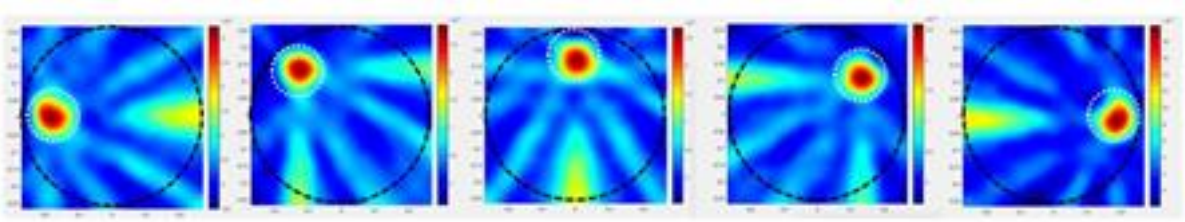

Figure 8: Preliminary image reconstructions using the smoothing algorithm. The 40 cm phantoms (white circle) is translated clockwise at 45° increments inside the imaging space (black circle). Experimental data.

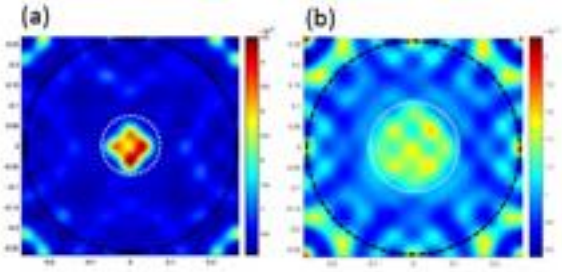

Figure 9: Preliminary image reconstructions using the positivity-imposing algorithm and experimental data. (a) is the 40 cm and (b) is the 60 cm phantom (white circles) at the centre of the imaging space (black circle).

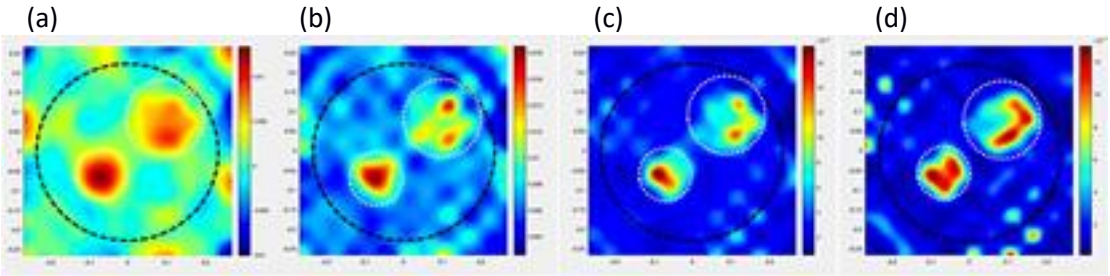

Figure 10: Preliminary image reconstructions of the same dual phantom comparing the smoothing (a) and positivity-constrained algorithm (b-d) near the converging point. Experimental data.

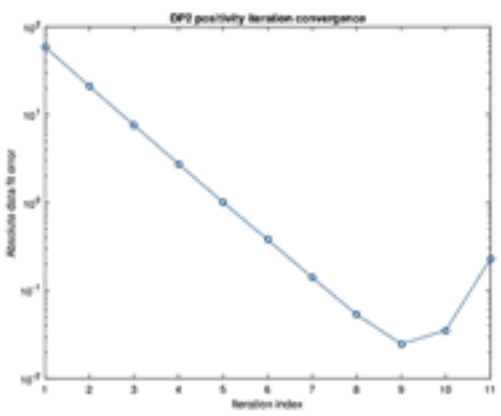

Figure 11: Data fit error versus iteration index during execution of the positivity-imposing algorithm while reconstructing experimental data from a dual phantom test.

7. Discussion & conclusions

The reconstructions depicted in Figure 7 and 8 show very good localisation of the plumes and good shape definition. The plume translation experiment (Figure 8) gives rise to reconstruction artefacts that are a consequence of the limited number of projections available. Nevertheless, these can be suppressed with further optimisation of the existing algorithms. The virtually predictable 'movement' of these artefacts in the imaging space as a function of the phantom's location indicates that all 126 measurement channels are performing within specifications and without significant deviations.

Figure 8a depicts a reconstruction using the positivity-imposing algorithm. A loss of the circular geometry of the actual concentration distribution can be seen and the edges appear 'square'. This effect is a consequence of the low-dimensional space projection step and is amplified by the positivity-imposing reconstruction algorithm. In other words, this effect is also present in reconstructions using the smoothness-imposing algorithm but suppressed due to the smoothing action.

In Figure 7c in the case of the dual phantom the fitting error is 30%. For the single 60 cm phantom in Figure 7b the fitting error is 22% whereas for the same phantom and using the positivity-constrained algorithm (Figure 9b) the error is 37%. In general, the smoothness-imposing algorithm appears to produce reconstructions that more faithfully represent the actual CO_2 distribution concentration. However, the relative fitting error is comparable and very good for both algorithms.

In this paper we have presented the first results generated by the CO_2 imaging system of project FLITES. The gaseous phantoms used to emulate the turbine engine exhaust introduced sufficient CO_2 to create a robust WMS signal from all the 126 installed beams thus demonstrating full operation of the tomography system and its sub-components: light source, opto-mechanical structures, data acquisition system, data conditioning algorithm, spectroscopic fitting algorithm and image reconstruction algorithm.

We have presented the first preliminary tomographic reconstructions using the smoothness-imposing and positivity-imposing reconstruction algorithms. The preliminary images show very good localisation of the gaseous phantoms and the smoothness-imposing algorithm faithfully represents the geometry of the concentration distribution that was introduced. The aim of the work to follow is to refine the data acquisition process, extend the image reconstruction process and prepare the system for installation in the engine test cell.

Acknowledgment

The authors are grateful to CIEMAT, a public research body assigned to the Spanish Ministry of Economy and Competitiveness, for providing gas supplies and assistance in conducting the experiments.

References

1. POLYDORIDES N., TSEKENIS S.-A., MCCANN HUGH, PRAT DANIEL ARCHILLA V., WRIGHT P. (2016), An efficient approach for limited-data chemical species tomography and its error bounds. Royal Society A: Mathematical, Physical and Engineering Sciences, 472.
2. WRIGHT P., MCCORMICK D., KLIMENT J., OZANYAN K., TSEKENIS S.-A., FISHER E., MCCANN H., ARCHILLA V., GONZÁLEZ-NÚÑEZ A., JOHNSON M., BLACK J., LENGDEN M., WILSON D., JOHNSTONE W., FENG Y., NILSSON J. (2016). Implementation of non-intrusive jet exhaust species distribution measurements within a test facility. Proc. IEEE Aerospace Conference 2016, 5-12 Mar 2016, Big Sky, Montana, USA.
3. WILSON D., ARMSTRONG I., LENGDEN M., JOHNSTONE W. (2014). In-situ measurement of combustion produced CO_2 in the 2 µm region, within a jet engine exhaust plume. Proc. Field Laser Applications in Industry and Research (FLAIR), 5-9 May 2014, Florence, Italy.
4. FENG Y., NILSSON J., JAIN S., MAY-SMITH T.C., SAHU J.K., JIA F., WILSON, D., LENGDEN M., JOHNSTONE W. (2014). LD-seeded thulium-doped fibre amplifier for CO_2 measurements at 2 µm. Proc. 6th Europhoton Conference (EPS-QEOD), 24-29 Aug 2014, Neuchâtel, Switzerland.
5. FISHER E, YANG Y, OUYPORNKOCHAGORN T, CHIGHINE A, TSEKENIS S-A, POLYDORIDES N, KLIMENTS J, WRIGHT P, WILSON D, LENGDEN M, PRAT V, JOHNSTONE W, MCCANN H. (2016). Data acquisition for multi-channel CST of aero-engine exhaust plume species and combustion diagnostics. Proc. 8th World Congress on Industrial Process Tomography (WCIPT8), 26-29 Sep 2016, Iguassu Falls, Brazil.
6. CHIGHINE A., FISHER E., TSEKENIS S.-A., MCCANN H. (2015). TDLAS using FPGA-based Lock-In detection for multi-channel Chemical Species Tomography. IEEE Sensors, Nov 2015, Busan, N. Korea.